

EXPERIMENTAL AND NUMERICAL MODELING OF THE HEAT GENERATION CHARACTERISTICS OF LITHIUM IRON PHOSPHATE BATTERY UNDER NAIL PENETRATION

Yanxin YIN¹, Tao ZHANG¹, Zuoqiang DAI¹, Tao WEI², Xiangyun QIU^{1,3,*}

¹Power & Energy Storage System Research Center, College of Mechanical and Electrical Engineering, Qingdao University, Qingdao, 266071, China

²School of Energy and Power, Jiangsu University of Science and Technology, Zhenjiang, 212003, China

³Weifang Juneng Battery Co., LTD., Weifang, 261021, China

*Corresponding author; Email: yunners@126.com; qiuxiangyun@qdu.edu.cn

This study conducted nail penetration tests on 20 Ah prismatic LiFePO₄ batteries and simulated the slow release of Joule heat and side reaction heat by combining a new thermal model with a parameter optimization method. The results indicate that the 50% and 80% SOC LiFePO₄ batteries only release Joule heat under penetration, while the side reaction heat is acquired under 100% SOC besides Joule heat. Moreover, approximately 56.4% of the stored electrical energy is converted into Joule heat, which accounts for the majority of the total heat production of 100% SOC LiFePO₄ battery under penetration, while side reaction heat accounts for only 6.4%. Furthermore, the exothermic side reactions of 100% SOC LiFePO₄ battery under penetration can be effectively suppressed when the electrical energy release ratio is less than 0.52, or the convection coefficient between the battery and its surroundings exceeds 12 W·m⁻²·K⁻¹. This numerical study expands the analysis of the heat generation characteristics of LiFePO₄ batteries during penetration and provides practical guidance for system safety design.

Key words: LiFePO₄ battery; penetration; simulation; Joule heat; side reaction heat

1. Introduction

Lithium-ion batteries (LIBs) are excellent carriers of electrical energy, providing reliable power for electric vehicles and energy storage systems [1, 2]. However, LIBs are prone to thermal runaway (TR) during extreme operating conditions such as overcharging, overheating, and mechanical collisions [3-5]. Reducing the TR risk has now become one of the major challenges due to the increasing size and capacity of single batteries. Among multitudinous types of LIBs, LiFePO₄ (LFP) batteries are considered to have the best resistance to thermal safety issues [6-9]. Nevertheless, several energy storage systems carrying LFP battery packs have been involved in fire accidents under charging, crash and even resting conditions, which has caused researchers to revisit the thermal safety

of LFP batteries.

Overheating [10-15], overcharging [16-19], and internal short circuit (ISC) [20, 21] are the three most common abuse issues encountered by LIBs. Overheating and overcharging both trigger TR by inputting energy into the battery from the outside, while ISC triggers TR by the release of their own energy. Many of the thermal safety incidents in LFP batteries are caused by ISC. Battery ISC has two primary causes: lithium dendrite piercing the separator during prolonged cycling [22], and metal parts piercing inside the battery after impact, crushing or penetration [23]. The latter can cause a rapid release of electrical energy, leading to exothermic side reactions and eventually resulting in battery TR. The nail penetration is often used to identify battery ISC and is an effective method for studying the short circuit safety of LIBs.

The heat generation characteristics are a critical research focus of the penetration test for LFP batteries. Huang *et al.* [21] concluded that the two primary heat sources for 18650 type LFP batteries under penetration are Joule heat (resulting from ISC) and side reaction heat (caused by the chemical reaction of battery materials). However, the authors did not provide a quantitative analysis of these heat sources. Building simulation models is an effective tool for conducting quantitative analysis [24-29], while most models are tailored to ternary LIBs and may not be universally applicable to LFP batteries. Furthermore, previous studies have typically assumed that the release rate of Joule heat caused by battery ISC is either constant [30, 31] or calculated using the Arrhenius formula [32, 33]. However, these methods are only suitable for the rapid release of electrical energy and may not accurately reflect the slow release of electrical energy that is often observed with high-security LFP batteries under penetration. Therefore, it is essential to undertake a quantitative study into the heat generation characteristics of LFP batteries under penetration, especially when it involves the slow release of electrical energy, for which currently there is no existing simulation model.

Therefore, penetration tests were conducted to investigate the TR characteristics of 20 Ah prismatic LFP batteries at different SOC levels (state of charges), including temperature, voltage and TR behavior. What's more, we proposed a new method of modeling the slow release of electrical energy from LFP batteries under penetration and integrated parameter optimization to enable precise quantitative calculations of Joule heat and side reaction heat.

2. Experimental

2.1 Lithium-ion battery samples

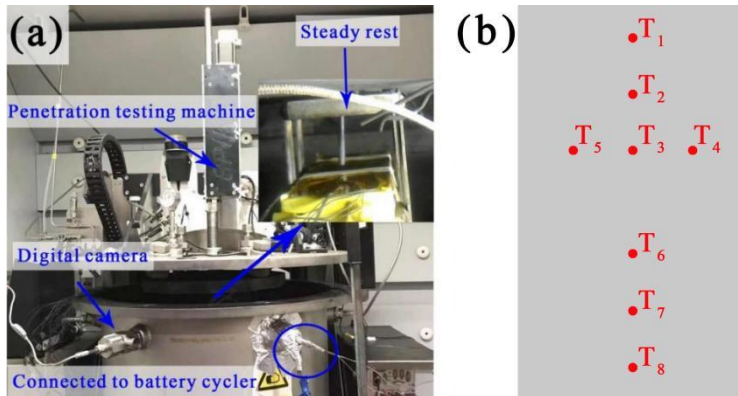
The tested sample battery is a commercial 20 Ah prismatic LiFePO_4 /graphite battery, and it is a new one with a flattened cell structure and an aluminum shell that is 0.6 mm thick. Details of the battery are presented in Tab. 1. The battery SOC levels used in the experiment were 50%, 80% and 100%, respectively. Before the penetration tests, each battery underwent four charge/discharge cycles at a constant current-constant voltage mode with a current magnitude of 0.5C. In the last discharge step, the batteries were discharged to the specified SOC.

Tab. 1 Some specific information of the tested LFP batteries.

Parameters	Specification
Cathode	Lithium iron phosphate
Anode	Graphite
Nominal capacity (Ah)	20
Maximum cut off voltage (V)	3.65
Minimum cut off voltage (V)	2.5
Nominal voltage (V)	3.2
Geometry (mm)	$24.5 \times 70.9 \times 121.8$
Mass (g)	447.9
Specific heat capacity ($\text{J} \cdot \text{kg}^{-1} \cdot \text{K}^{-1}$)	1100

2.2 Penetration tests

The penetration bench used for this test is shown in Fig. 1(a), which was provided by the accelerating rate calorimetry (ARC) device manufactured by THT. The battery was placed flat on the steady rest, and a 4 mm diameter stainless steel nail was driven through the centre of the battery at a speed of $10 \text{ mm} \cdot \text{s}^{-1}$ until it penetrated the battery and then stopped, and the working temperature of the battery was 30°C . Eight K-type thermocouples (T_1 - T_8) were arranged on the battery surface, as shown in Fig. 1(b), to collect temperature data. These thermocouples divided the large surface of the battery into four regions: the area near the safety valve (T_1 , T_2), the area near the stainless steel nail (T_3 , T_6), the area away from both the safety valve and stainless steel nail (T_7 , T_8), and the area at a moderate distance from the safety valve and stainless steel nail (T_4 , T_5). Throughout the test, the Neware battery cycler was utilized to collect voltage data, while the TR behavior was captured through a digital camera.

**Fig. 1 (a) Setting of penetration test and (b) arrangement of thermocouples.**

2.3 Accelerating rate calorimetry test

The ARC test was conducted to measure the onset temperature of self-heating in the LFP battery at 100% SOC. The test result obtained through a typical “heat-wait-search” testing program [34] is shown in Fig. 2. It can be seen that the onset temperature of self-heating (T_{SH}) in the battery is 90.3°C ,

which indicates that the solid electrolyte interface (SEI) begins to decompose at around 90 °C. It is worth noting that 90.3 °C is the temperature detectable by the ARC equipment, and the actual decomposition temperature of the SEI may be much lower than this. For instance, Wang *et al.* [35] obtained a decomposition temperature of 61 °C for the SEI through C80 experiments. However, at this temperature, the heat generation rate from the decomposition of the SEI is very low, resulting in a temperature rise rate of less than 0.02 °C·min⁻¹, which can be ignored. Therefore, the authors set the decomposition temperature of the SEI as 90 °C in this paper.

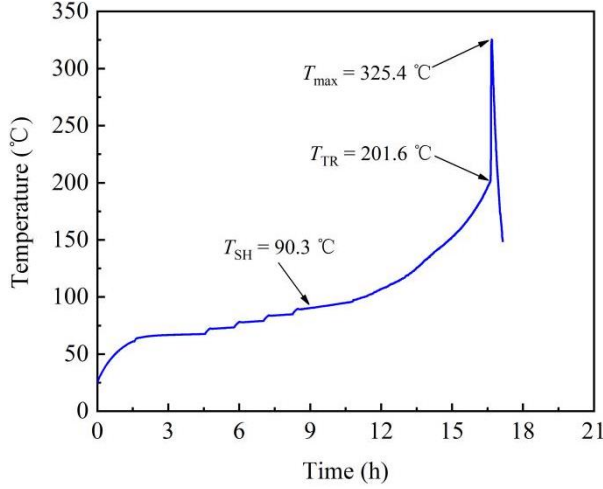


Fig. 2 The temperature curves of ARC test.

3. Numerical model

3.1 Heat generation

The total heat production rate (Q_{Tot}) of the LFP battery under penetration is composed of Q_{Jou} and Q_{Sid} as shown in Eq. (1), where Q_{Jou} and Q_{Sid} are the Joule heat rate and side reaction heat rate, respectively. The calculation methods of Q_{Jou} and Q_{Sid} are described in detail in section 4.3.

$$Q_{Tot} = Q_{Jou} + Q_{Sid} \quad (1)$$

3.2 Heat transfer

The LFP battery geometry model, depicted in Fig. 3, consists of two homogeneous solid components: the battery core and the 0.8 mm thick battery shell, which were built in Comsol Multiphysics 5.6 and contained a total of 104452 grid elements. The thermal property parameters of these components are presented in Tab. 2. Three heat transfer paths are considered: heat transfer within the solid component, governed by Eq. (2) [23]; heat transfer between the shell and the core, which follows Eq. (3) (the thin structure and gap between the shell and the core are simplified as an equivalent thermal resistance layer) [31]; and heat transfer at the boundary, including thermal convection and radiation, calculated by Eq. (4) [25]. The nomenclature table provides definitions for the variables and parameters in Eq. (2)-(4), and the heat transfer parameters are shown in Tab. 3. The value of ε (radiation heat transfer coefficient) in this paper is set as 0.3 according to the Ref. [36]. Additionally, Jia *et al.* [37] calibrate the model parameters of the TR model and suggest that the h

(heat convective coefficient) should be set to $10 \text{ W} \cdot \text{m}^{-2} \cdot \text{K}^{-1}$ when ε is 0.3. Therefore, the value of h in this paper is set as $10 \text{ W} \cdot \text{m}^{-2} \cdot \text{K}^{-1}$.

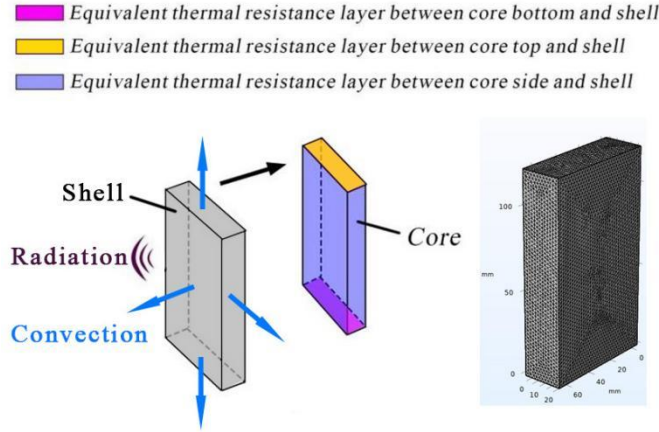


Fig. 3 The heat transfer and grid schematic of the model.

Tab. 2 Parameter values of the model components.




Components	$\rho \text{ (kg} \cdot \text{m}^{-3}\text{)}$	$C_p \text{ (J} \cdot \text{kg}^{-1} \cdot \text{K}^{-1}\text{)}$	$\lambda \text{ (W} \cdot \text{m}^{-1} \cdot \text{K}^{-1}\text{)}$
Shell	2700	900	160
Core	2070	1100	$\lambda_x = \lambda_z = 15.3$ [26] $\lambda_y = 0.84$ [26]

$$\rho C_p \frac{\partial T}{\partial \tau} = q_v + \frac{\partial}{\partial x} \left(\lambda_x \frac{\partial T}{\partial x} \right) + \frac{\partial}{\partial y} \left(\lambda_y \frac{\partial T}{\partial y} \right) + \frac{\partial}{\partial z} \left(\lambda_z \frac{\partial T}{\partial z} \right) \quad (2)$$

$$-\lambda \frac{\partial T}{\partial n} = \frac{\lambda_{layer}}{\delta_{layer}} (T_1 - T_2) \quad (3)$$

$$-\lambda \frac{\partial T}{\partial n} = h(T_0 - T_\infty) + \varepsilon \sigma (T_0^4 - T_\infty^4) \quad (4)$$

Tab. 3 Setting of heat transfer parameters.

Colour	Description	$\delta \text{ (mm)}$	$\lambda \text{ (W} \cdot \text{m}^{-1} \cdot \text{K}^{-1}\text{)}^a$	$h \text{ (W} \cdot \text{m}^{-2} \cdot \text{K}^{-1}\text{)}$	ε
	Equivalent thermal resistant between core side and shell	1	0.28	/	/
	Equivalent thermal resistant between core top and shell	4	0.025	/	/
	Equivalent thermal resistant between core bottom and shell	2	0.025	/	/
h	Heat convection coefficient surrounding the battery module	/	/	10[37]	/
ε	The radiation heat transfer coefficient	/	/	/	0.3[36]

^aThe heat conductivity of the equivalent thermal resistant layer.

4. Results and discussion

4.1 Thermal runaway behavior

Fig. 4(a) and 4(b) show the TR behavior of 50% and 80% SOC LFP batteries under penetration, respectively, where no visible fire or smoke appears, and the battery shell remains intact with no visible deformation. However, as shown in Fig. 4(c), a large amount of smoke was observed during the testing of the 100% SOC LFP battery (marked by the red circle). Besides, the peeling off of the insulation tape on the battery shell, marked by the blue circle, indicates that the shell underwent severe deformation. The aforementioned phenomenon suggests that the LFP battery at 100% SOC exhibits the most severe TR behavior under penetration when compared to those at 50% and 80% SOC. This is attributed to the fact that the 100% SOC LFP battery releases a greater amount of electrical energy during penetration, resulting in a higher battery temperature. As a consequence, more exothermic side reactions are triggered, generating more gas and leading to severe deformation of the battery.

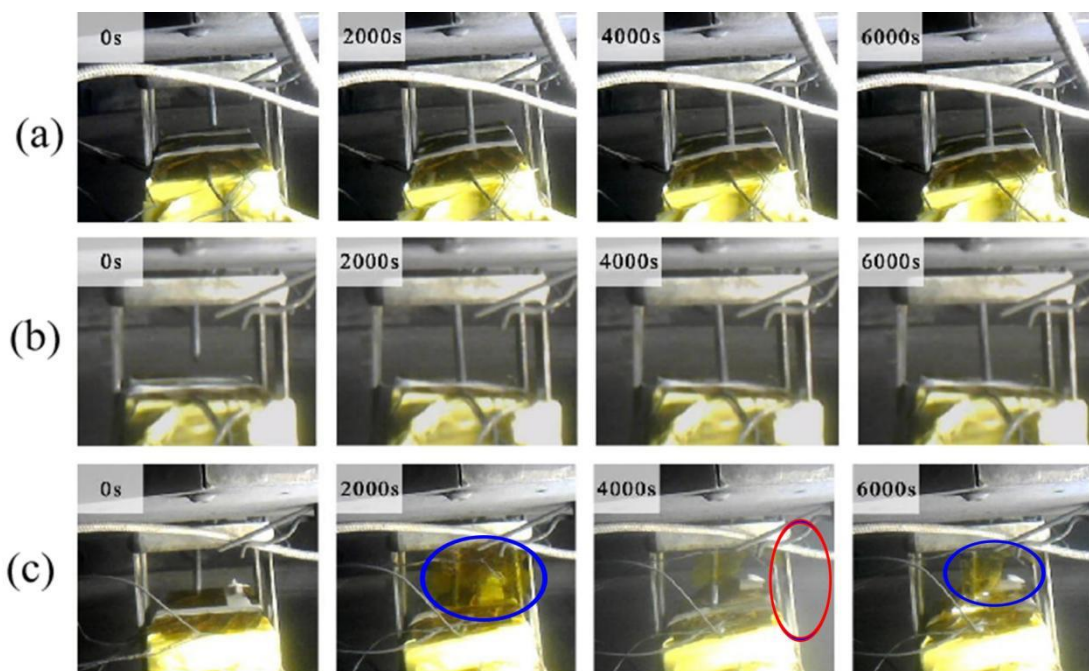


Fig. 4 Images of TR behavior of (a) 50%, (b) 80% and (c) 100% SOC LFP batteries under penetration.

4.2 Temperature and voltage characteristics

Fig. 5(a)-5(c) show the temperature and voltage curves of LFP batteries with different SOC levels under penetration. The temperature curve fluctuations are caused by the deformation of the battery shell when the nail penetrates the battery interior, which influences the tightness between the thermocouple and the battery surface. However, this does not significantly impact the test results. In the case of the 100% SOC LFP battery, the sharp temperature drops observed in the T_3 and T_5 curves suggest poor contact between these thermocouples and the battery surface. Therefore, their data was excluded from subsequent calculations of maximum temperature difference and average temperature. LFP batteries with different SOC levels exhibit a consistent temperature trend. When the nail punctures the

separator, battery ISC occurs, leading to the release of electrical energy and a nearly linear increase in battery temperature at the beginning of the test. Subsequently, the temperature rise rate gradually decreases as the Joule heat release rate reduces. Once the heat generation rate becomes lower than the heat dissipation rate, the battery temperature begins to decrease. The maximum temperature recorded for the 100% SOC LFP battery is 120.6 °C, whereas for the 80% and 50% SOC LFP batteries it is 89.4 °C and 64.9 °C, respectively, which are lower than the initial decomposition temperature (~ 90 °C) of the SEI detectable by accelerating rate calorimeter [5]. This indicates that the 50% and 80% SOC LFP batteries experience almost no side reaction under penetration, which also accounts for the absence of observable smoke in Fig. 4(a) and 4(b). Different from the rapid voltage drop observed in most previous penetration studies, the voltage of the LFP batteries in this study decreased at a very slow rate, taking more than 4000 seconds to drop from above 3 V to 1 V. For commercial Li-ion batteries, some functional ceramic materials with higher melting points are coated on the surface of PE or PP substrates to enhance the thermal stability of separators [38, 39]. In the nail penetration test, the colloidal functional materials expand following the direction of the instant impact force and fill the space around the wound with the help of a viscous force. Meanwhile, very little change in the structure at the wound can be observed because of a stronger interface adhesion between the separator and electrodes, as well as the degree of short circuit is greatly reduced [40-43]. Besides, on account of the good ductility of the positive material, it wraps around the aluminum foil after being pierced by the nail, preventing direct contact between the nail and the foil. Additionally, the high resistance formed by its poor electronic conductivity hinders the propagation of electrons to the aluminum foil [44]. Therefore, only a small portion of the positive material surrounding the nail is involved in the internal short circuit after nail penetration, resulting in a gradual decrease in voltage rather than a rapid drop caused by a widespread short circuit. This slow voltage drop indicates a slow release of electrical energy, as demonstrated by the fact that the battery's temperature does not reach its maximum value until long after penetration. Furthermore, the temperature curve near the maximum value is relatively flat, rather than showing the “peak” shape frequently reported by researchers in the field [20-22].

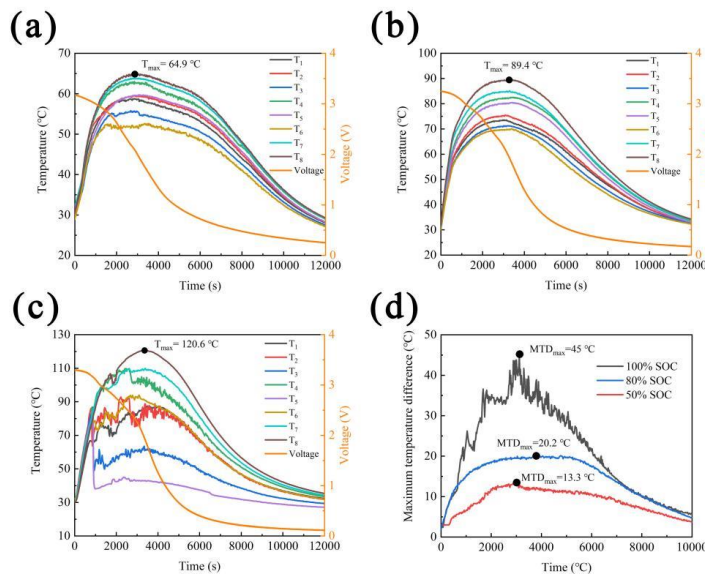


Fig. 5 Temperature distribution and voltage curve of (a) 50%, (b) 80% and (c) 100% SOC LFP batteries under penetration. (d) Maximum temperature difference of LFP batteries under penetration.

Fig. 5(d) shows the maximum temperature difference (MTD) of the LFP batteries under penetration. The MTD of the LFP battery with 100% SOC is significantly higher than both the 80% and 50% SOC batteries, indicating that the 100% SOC LFP battery exhibits the most drastic TR behavior. The battery temperature distribution is shown in Fig. 6. There are two main factors that cause uneven temperature distribution on the battery surface. The first factor is that the high-temperature gas generated by side reactions takes away a large amount of heat through the ruptured safety valve, resulting in a lower temperature at the top of the battery. The second factor is that heat conduction between the battery and the nail causes a lower temperature in the middle of the battery. Therefore, the highest temperature appears in the lower part of the battery far away from the safety valve and the nail, while the location of the lowest temperature is related to the SOC. When the battery SOC is 50% and 80%, according to the analysis in section 4.1, no gas is generated in the battery and the influence of the first factor can be ignored, while the second factor causes the lowest temperature to appear in the middle of the battery close to the nail as shown in Fig. 6(a). When the battery SOC is 100%, Fig. 4(c) shows that a large amount of gas is generated in the battery. The two factors jointly play a role, and the test results in Fig. 5(c) show that the effect of the first factor is more pronounced, leading to the lowest temperature appearing at the top of the battery near the safety valve as shown in Fig. 6(b).

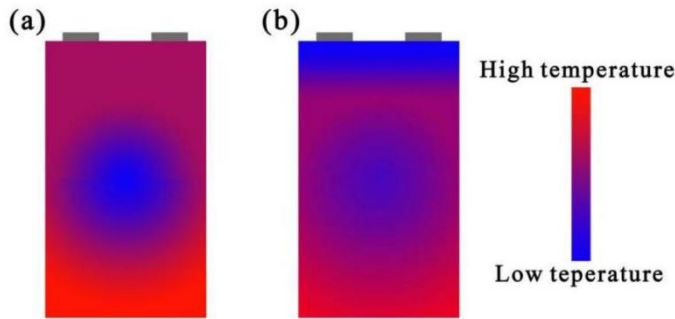


Fig. 6 Temperature distribution diagram of (a) 50%, 80% and (b) 100% SOC LFP batteries under penetration.

4.3 Simulation of joule heat rate (Q_{Jou}) and side reaction heat rate (Q_{Sid})

The piercing of stainless steel nail in LFP battery will lead to battery ISC and trigger the release of Joule heat, which increases the temperature and even triggers exothermic side reactions. Therefore, conducting accurate quantitative analysis of these two heat sources provides a better understanding of the thermal behavior of LFP batteries during penetration.

The analysis in section 4.2 shows that 50% SOC LFP battery releases only Joule heat without side reaction heat under penetration, so this case is used to show how to simulate the Joule heat rate. The voltage curve in Fig. 5(a) is normalized and then fitted as an exponential function, denoted as $E(t)$, as shown in Fig. 7(a). Here, the Joule heat rate (Q_{Jou}) is described by Eq. (5), where R_{Jou} is defined as the release rate function of Joule heat, and η is the proportion of stored electrical energy converted to Joule heat. The meanings of other parameters and variables in Eq. (5) are shown in nomenclature table.

$$\begin{cases} Q_{Jou} = \eta \cdot SOC \cdot \frac{3600s \cdot V \cdot C}{V_c} \cdot R_{Jou} \\ R_{Jou} = -\frac{dE(t)}{dt} \end{cases} \quad (5)$$

The total heat production rate of the 50% SOC LFP battery under penetration is simulated by taking Eq. (5) into Eq. (1), where the side reaction heat rate (Q_{Sid}) is 0. In order to accurately calculate the released electrical energy, the model parameter η in Eq. (5) is determined by the SNOPT optimization method supplied by Comsol Multiphysics 5.6. The optimization equation is shown in Eq. (6), where θ is the set of optimization parameters, T_{exp} is the average temperature measured by thermocouples T_1 - T_8 , and T_{sim} is the simulated temperature. The optimization goal is to minimize the value of function $S(\theta)$ within the given parameter range. The initial value, optimization range and optimization result of parameter η are shown in Tab. 4. It can be seen that about 56.4% of the stored electrical energy is released as Joule heat. Fig. 8(a) shows the comparison of the average temperature obtained from the penetration test (blue curve) and that obtained from the simulation model (orange curve). The high degree of concurrence between the two curves indicates that the established heat generation model is highly accurate. The simulated temperature curve of 80% SOC LFP battery under penetration can also be obtained using the method described above. In this case, η takes 0.564 directly without parameter optimization. Fig. 7(b) shows the fitting result of the voltage curve of 80% SOC LFP battery under penetration, and Fig. 8(b) indicates that the difference between the simulated and experimental temperature curves is small.

$$S(\theta) = \sum (T_{exp} - T_{sim})^2 \quad (6)$$

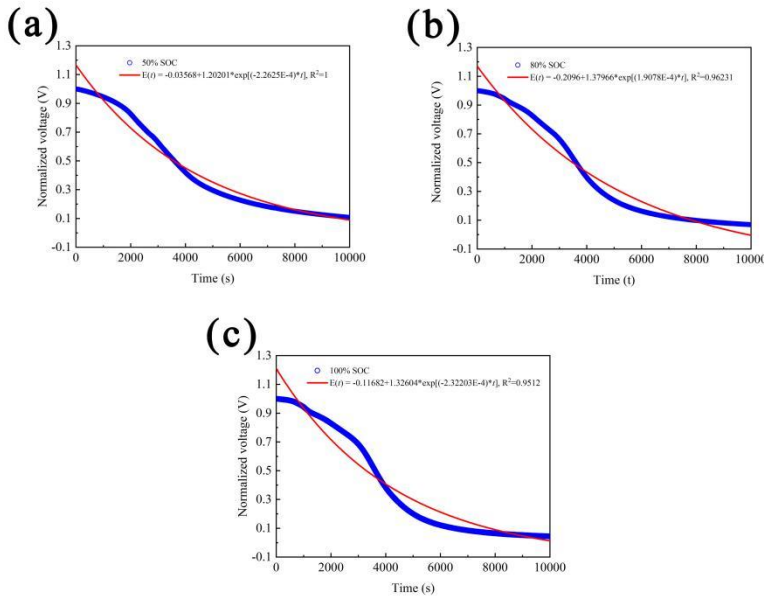


Fig. 7 Normalization and exponential function fitting of voltage curve of (a) 50%, (b) 80% and (c) 100% SOC LFP batteries under penetration.

Tab. 4 Initial values, optimization range and optimization results of parameters.

Parameters	Initial values	Ranges [4]	Results
η	0.6	0~1	0.564
$A_{Sid} (1 \cdot s^{-1})$	9.6×10^{14}	$2.5 \times 10^{13} \sim 1.667 \times 10^{15}$	6×10^{14}
$E_{Sid} (J \cdot kg^{-1})$	0.98×10^5	$2.57 \times 10^5 \sim 1.714 \times 10^6$	0.96×10^6

The maximum temperature (120 °C) reached by the 100% SOC LFP battery under penetration is sufficient to trigger the decomposition and regeneration of the SEI film[45, 46]. Thus, the 100% SOC LFP battery generates both Joule heat and side reaction heat under penetration. The Joule heat is simulated similarly to the 50% SOC LFP battery, and Fig. 7(c) shows the fitting result of the voltage curve of 100% SOC LFP battery under penetration. In this case, η takes 0.564 directly without parameter optimization. The side reaction heat is calculated by the Arrhenius formula as shown in Eq. (7) [32], where $W = 263.1 \text{ kg} \cdot \text{m}^{-3}$ is the mass and $E_a = 1.35\text{E}5 \text{ J} \cdot \text{mol}^{-1}$ [47]. The meanings of parameters and variables in Eq. (7) are shown in nomenclature table.

$$\begin{cases} R_{Sid} = A_{Sid} \cdot \exp\left(-\frac{E_a}{RT}\right) \cdot c \\ \frac{dc}{dt} = -R_{Sid} \\ Q_{Sid} = E_{Sid} \cdot W \cdot R_{Sid} \end{cases} \quad (7)$$

The unknown parameters A_{Sid} and E_{Sid} are obtained using the aforementioned SNOPT optimization method, with their initial values, optimization range and optimization results shown in Tab. 4. As shown in Fig. 8(c), the temperature profile acquired from the test closely resembles the simulation results, indicating the high precision of the developed heat generation model. The reason why the experimental and simulation curves do not fully overlap is that the simulation model did not consider the heat conduction between the battery and the nail, as well as some of the heat being carried away by the high-temperature gas ejected from the safety valve. Additionally, the uneven distribution of temperature on the battery surface can also have an impact on the accuracy of the model. By using the SNOPT optimization method to adjust the model parameters, the impact of the aforementioned uncertainty factors on the model's accuracy can be minimized as much as possible. The Joule heat (H_{Jou}) and side reaction heat (H_{Sid}) of the 100% SOC LFP battery under penetration are calculated by Eq. (8) and Eq. (9), respectively, with $t = 10000 \text{ s}$. The calculation gives $H_{Jou} = 140413 \text{ J}$ and $H_{Sid} = 9678 \text{ J}$. It can be seen that the Joule heat is the main heat source, while the side reaction heat only accounts for 6.4% of the total heat production.

$$H_{Jou} = \int \int_{V_c} Q_{Jou} dV_c dt \quad (8)$$

$$H_{Sid} = \int \int_{V_c} Q_{Sid} dV_c dt \quad (9)$$

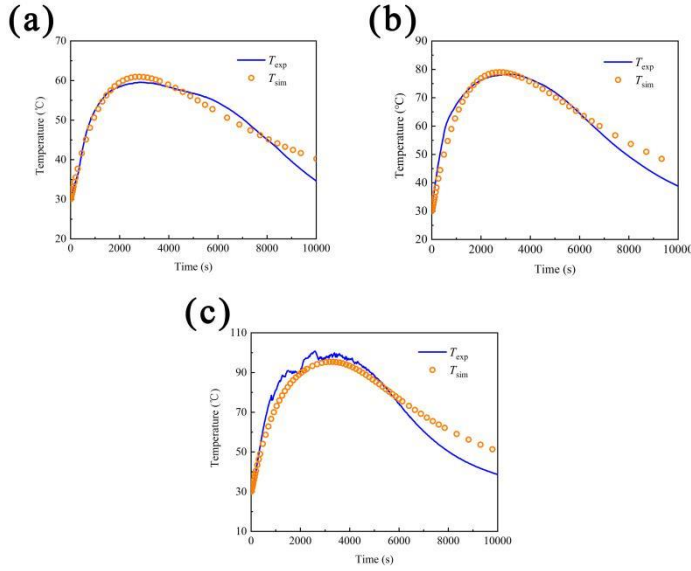


Fig. 8 Comparison of experimental and simulated average temperature curves. (a) 50%, (b) 80% and (c) 100% SOC.

4.4 Parameter analysis of the simulation model

The above results indicate that reducing the amount of electrical energy released can effectively reduce the heat production of LFP battery under penetration. This is because the release of electrical energy not only directly raises the battery temperature, but also induces exothermic side reactions that further increase the battery temperature. In addition, the heat convection has been confirmed to have an significant effect on the temperature of the battery under extreme operating conditions [2, 31, 47]. Therefore, the effect of the percentage of electrical energy released (η) and the convective coefficient (h) on the temperature of 100% SOC LFP battery under penetration is investigated by the simulation model. Fig. 9 shows that the battery temperature decreases as η drops or h rises. In particular, when η is less than 0.52 or h is greater than $12 \text{ W}\cdot\text{m}^{-2}\cdot\text{K}^{-1}$, the maximum battery temperature remains below 90°C , which is the temperature threshold for exothermic side reactions. Under such conditions, the side reactions are effectively suppressed, thus preventing further heat generation and subsequent temperature rise.

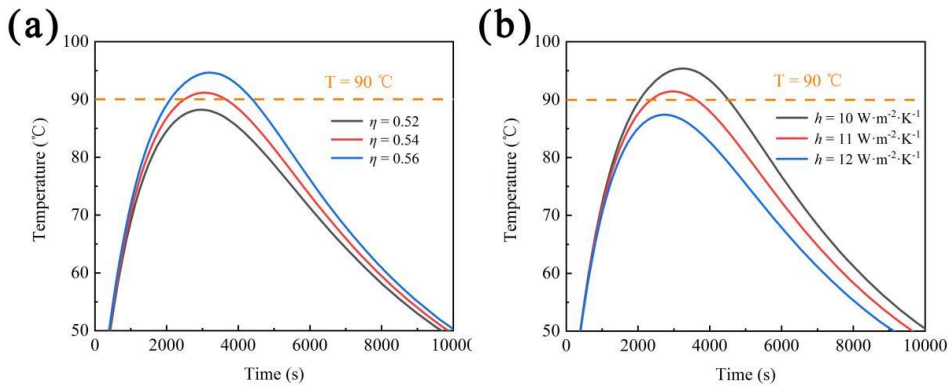


Fig. 9 The effect of (a) η and (b) h on the temperature of 100% SOC LFP battery under penetration.

5. Conclusions

In this paper, penetration tests are carried out on the 20 Ah prismatic LFP batteries with different SOC. It is found that the 50% and 80% SOC LiFePO₄ batteries only release Joule heat under penetration, while the side reaction heat is acquired under 100% SOC besides Joule heat, resulting in further temperature rise, gas release and battery deformation. Furthermore, we present an innovative method for simulating the heat generation characteristics of the LFP battery under penetration. The simulation results reveal that approximately 56.4% of the stored electrical energy in the battery is converted to Joule heat, which accounts for 93.6% of the total heat production of 100% SOC LFP battery under penetration. Only 6.4% of the heat generated is attributed to side reactions. Moreover, the battery exhibits high resistance to thermal runaway, as the maximum temperature that the battery can reach under penetration is lower than 90 °C (the temperature threshold for exothermic side reactions) when the electrical energy release ratio (η) is less than 0.52 or the convective coefficient (h) is greater than 12 W·m⁻²·K⁻¹.

Acknowledgement

This work was supported by the Science and Technology Small and Medium-sized Enterprises Innovation Ability Enhancement Project of Shandong Province (2022TSGC1252, 2023TSGC0754).

Nomenclature	
Acronyms	
LIBs	Lithium-ion batteries
TR	Thermal runaway
LFP	LiFePO ₄
ISC	Internal short circuit
SOCs	State of charges
ARC	Accelerating rate calorimetry
SEI	Solid electrolyte interface
Variable or parameter	
Q_{Tot}	The total heat production rate (W)
Q_{Jou}	The Joule heat rate (W)
Q_{Sid}	The side reaction heat rate (W)
C_p	The specific heat capacity (J·kg ⁻¹ ·K ⁻¹)
$\frac{\partial T}{\partial \tau}$	The temperature rise rate (K·s ⁻¹)
$\frac{\partial T}{\partial x}, \frac{\partial T}{\partial y}, \frac{\partial T}{\partial z}, \frac{\partial T}{\partial n}$	The temperature gradient (K·m ⁻¹)
q_v	The volumetric heat generation rate (W·m ⁻³)
T_1/T_2	The temperature at the surface of adjacent component (K, °C)
T_0	The temperature at the surface of the solid component (K, °C)
T_∞	The ambient temperature (K, °C)

h	The equivalent thermal contact resistance, or the heat convection coefficient ($\text{W} \cdot \text{m}^{-2} \cdot \text{K}^{-1}$)
V	The nominal voltage of battery (V)
C	The capacity of battery (Ah)
V_c	The volume of the core (m^3)
R_{Sid}	The reaction rate of side reactions (s^{-1})
A_{Sid}	The pre-exponential factor (s^{-1})
E_a	The activation energy ($\text{J} \cdot \text{mol}^{-1}$)
R	The gas constant ($\text{J} \cdot \text{mol}^{-1} \cdot \text{K}^{-1}$)
c	The normalized concentration of reactants (1)
E_{Sid}	The side reaction unit weight heat generation rate ($\text{J} \cdot \text{kg}^{-1}$)
W	The mass of reactant (kg)
H_{Jou}	The total Joule heat generated by LFP battery (J)
H_{Sid}	The total side reaction heat generated by LFP battery (J)
Greek letters	
ρ	The Density of solid components ($\text{kg} \cdot \text{m}^{-3}$)
$\lambda_x, \lambda_y, \lambda_z$	The heat conductivity in direction of x, y and z ($\text{W} \cdot \text{m}^{-1} \cdot \text{K}^{-1}$)
λ	The heat conductivity of all solid components ($\text{W} \cdot \text{m}^{-1} \cdot \text{K}^{-1}$)
λ_{layer}	The heat conductivity of the equivalent thermal resistant layer ($\text{W} \cdot \text{m}^{-1} \cdot \text{K}^{-1}$)
δ_{layer}	The thickness of the equivalent thermal resistant layer (mm)
ε	The emissivity coefficient (1)
σ	The Stefan-Boltzmann constant ($\text{W} \cdot \text{m}^{-2} \cdot \text{K}^{-4}$)
η	The proportion of stored electrical energy converted to Joule heat (1)

References

- [1] Peng, Y., *et al.*, A New Exploration of the Fire Behaviors of Large Format Lithium Ion Battery, *Journal of Thermal Analysis and Calorimetry*, 139 (2020), 2, pp. 1243-1254 DOI: 10.1007/s10973-019-08459-3
- [2] Zhang, T., *et al.*, The Characteristics of Thermal Runaway And Its Propagation of Large-format LiFePO₄ Batteries Under Overcharging and Overheating Conditions, *Bulletin of The Chemical Society of Japan*, 95 (2022), 11, pp. 1626-1637 DOI: 10.1246/bcsj.20220242
- [3] Narayanasamy, M.P., *et al.*, Heat Transfer Analysis of Looped Micro Heat Pipes with Graphene Oxide Nanofluid for Li-ion Battery, *Thermal Science*, 25 (2021), 1, pp. 395-405 DOI: 10.2298/TSCI200125218M
- [4] Li, J., *et al.*, Lithium-ion Battery Overcharging Thermal Characteristics Analysis and an Impedance-based Electro-thermal Coupled Model Simulation, *Applied Energy*, 254 (2019), pp. 113574 DOI: 10.1016/j.apenergy.2019.113574
- [5] Spotnitz, R., Franklin, J., Abuse Behavior of High-power, Lithium-ion cells, *Journal of Power Sources*, 113 (2003), 1, pp. 81-100 DOI: 10.1016/S0378-7753(02)00488-3
- [6] Mastali, M., *et al.*, Electrochemical-thermal Modeling and Experimental Validation of Commercial Graphite/LiFePO₄ Pouch Lithium-ion Batteries, *International Journal of Thermal Sciences*, 129 (2018), pp. 218-230 DOI: 10.1016/j.ijthermalsci.2018.03.004

- [7] Huang, Y., *et al.*, Numerical Study on the Use of Emergency Cooling During the Process of Lithium-ion Battery Thermal Runaway, *Journal of Electrochemical Energy Conversion and Storage*, 19 (2022), 3, pp. 030909 DOI:10.1115/1.4054016
- [8] Wang, Z., *et al.*, Overcharge-to-thermal-runaway Behavior and Safety Assessment of Commercial Lithium-ion Cells with Different Cathode Materials: A Comparison Study, *Journal of Energy Chemistry*, 55 (2021), pp. 484-498 DOI: 10.1016/j.jechem.2020.07.028
- [9] Said, A.O., *et al.*, Experimental Investigation of Cascading Failure in 18650 Lithium Ion Cell Arrays: Impact of Cathode Chemistry, *Journal of Power Sources*, 446 (2020), pp. 227347 DOI: 10.1016/j.jpowsour.2019.227347
- [10] Wang, S., *et al.*, Study of the Temperature and Flame Characteristics of Two Capacity LiFePO₄ Batteries in Thermal Runaway. *Journal of The Electrochemical Society*, 165 (2018), 16, pp. A3828-A3836 DOI: 10.1149/2.0531816jes
- [11] Mao, B., *et al.*, Thermal Runaway and Fire Behaviors of a 300 Ah Lithium Ion Battery with LiFePO₄ as Cathode, *Renewable & Sustainable Energy Reviews*, 139 (2021), pp. 110717 DOI: 10.1016/j.rser.2021.110717
- [12] Liu, P., *et al.*, Experimental Study on Thermal Runaway and Fire Behaviors of Large Format Lithium Iron Phosphate Battery, *Applied Thermal Engineering*, 192 (2021), pp. 116949 DOI: 10.1016/j.applthermaleng.2021.116949
- [13] Peng, Y., *et al.*, A Comprehensive Investigation on the Thermal and Toxic Hazards of Large Format Lithium-ion Batteries with LiFePO₄ Cathode, *Journal of Hazardous Materials*, 381 (2020), pp. 120916 DOI: 10.1016/j.jhazmat.2019.120916
- [14] Liu, P., *et al.*, Thermal Runaway and Fire Behaviors of Lithium Iron Phosphate Battery Induced by Over Heating, *Journal of Energy Storage*, 31 (2020), pp. 101714 DOI: 10.1016/j.est.2020.101714
- [15] Wang, Q., *et al.*, Combustion Behavior of Lithium Iron Phosphate Battery Induced by External Heat Radiation, *Journal of Loss Prevention in the Process Industries*, 49 (2017), pp. 961-969 DOI: 10.1016/j.jlp.2016.12.002
- [16] Gao, F., *et al.*, Study on Thermal Runaway Process of LiFePO₄/C Batteries, *Environment Earth Science*, 631 (2021), pp. 012105 DOI: 10.1088/1755-1315/631/1/012105
- [17] Zhang, Z., *et al.*, Temperature Characteristics of Lithium Iron Phosphatepower Batteries Under Overcharge, *International Journal of Energy Research*, 44 (2020), 14, pp. 11840-11851 DOI: 10.1002/er.5824
- [18] Sun, L., *et al.*, Comparative Study on Thermal Runaway Characteristics of Lithium Iron Phosphate Battery Modules Under Different Overcharge Conditions, *Fire Technology*, 56 (2020), 4, pp. 1555-1574 DOI: 10.1007/s10694-019-00942-5
- [19] Wang, C., *et al.*, Thermal Runaway Behavior and Features of LiFePO₄/graphite Aged Batteries Under Overcharge, *International Journal of Energy Research*, 44 (2020), 7, pp. 5477-5487 DOI: 10.1002/er.5298
- [20] Wang, H., *et al.*, Mechanical Abuse Simulation and Thermal Runaway Risks of Large-format Li-ion Batteries, *Journal of Power Sources*, 342 (2017), pp. 913-920 DOI: 10.1016/j.jpowsour.2016.12.111
- [21] Huang, Z., *et al.*, Thermal Runaway Behavior of Lithium Iron Phosphate Battery During Penetration, *Fire Technology*, 56 (2020), 6, pp. 2405-2426 DOI: 10.1007/s10694-020-00967-1

- [22] Bhattacharyya, R., *et al.*, In Site NMR Observation of the Formation of Metallic Lithium Micro Structures in Lithium Batteries, *Nature Materials*, 9 (2010), pp. 504-510 DOI: 10.1038/nmat2764
- [23] Ren, D., *et al.*, Investigating the Relationship Between Internal Short Circuit and Thermal Runaway of Lithium-ion Batteries Under Thermal Abuse Condition, *Energy Storage Materials*, 34 (2021), pp. 563-573 DOI: 10.1016/j.ensm.2020.10.020
- [24] Liu, B., *et al.*, Integrated Computation Model of Lithium-ion Battery Subject to Nail Penetration, *Applied Energy*, 183 (2016), pp. 278-289 DOI: 10.1016/j.apenergy.2016.08.101
- [25] Lai, X., *et al.*, Investigation of Thermal Runaway Propagation Characteristics of Lithium-ion Battery Modules Under Different Trigger Modes, *International Journal of Heat Mass Transfer*, 171 (2021), pp. 121080 DOI: 10.1016/j.ijheatmasstransfer.2021.121080
- [26] Zhao, W., *et al.*, Modeling Nail Penetration Process in Large-Format Li-ion Cells, *Journal of The Electrochemical Society*, 162 (2015), 1, pp. A207-A217 DOI: 10.1149/2.1071501jes
- [27] Wang, S., *et al.*, A Simulation on Safety of LiFePO₄/C Cell Using Electrochemical Thermal Coupling Model, *Journal of Power Sources*, 244 (2013), pp. 101-108 DOI: 10.1016/j.jpowsour.2013.03.100
- [28] Bugrynieca, P.J., *et al.*, Computational Modelling of Thermal Runaway Propagation Potential in Lithium Iron Phosphate Battery Packs, *Energy Reports*, 6 (2020), pp. 189-197 DOI: 10.1016/j.egyr.2020.03.024
- [29] Macdonald, M.P., *et al.*, Thermal Runaway in a Prismatic Lithium Ion Cell Triggered by a Short Circuit, *Journal of Energy Storage*, 40 (2021), pp. 102737 DOI: 10.1016/j.est.2021.102737
- [30] Ren, D., *et al.*, An Electrochemical-thermal Coupled Overcharge-to-thermal-runaway Model for Lithium Ion Battery, *Journal of Power Sources*, 364 (2017), pp. 328-340 DOI: 10.1016/j.jpowsour.2017.08.035
- [31] Jin, C., *et al.*, Model and Experiments to Investigate Thermal Runaway Characterization of Lithium-ion Batteries Induced by External Heating Method, *Journal of Power Sources*, 504 (2021), pp. 230065 DOI: 10.1016/j.jpowsour.2021.230065
- [32] Coman, P.T., *et al.*, Modelling Li-ion Cell Thermal Runaway Triggered by an Internal Short Circuit Device Using an Efficiency Factor and Arrhenius Formulations, *Journal of Electrochemical Society*, 164 (2017), 4, pp. A587-A593 DOI: 10.1149/2.0341704jes
- [33] Coman, P.T., *et al.*, Numerical Analysis of Heat Propagation in a Battery Pack Using a Novel Technology for Triggering Thermal Runaway, *Applied Energy*, 203 (2017), pp. 189-200 DOI: 10.1016/j.apenergy.2017.06.033
- [34] Röder, P., *et al.*, A Detailed Thermal Study of a Li[Ni_{0.33}Co_{0.33}Mn_{0.33}]O₂/LiMn₂O₄-based Lithium Ion Cell by Accelerating Rate and Differential Scanning Calorimetry, *Journal of Power Sources*, 248 (2014), pp. 978-987 DOI: 10.1016/j.jpowsour.2013.09.146
- [35] Wang, Q., *et al.*, Thermal Behavior of Lithiated Graphite with Electrolyte in Lithium-Ion Batteries, *Journal of The Electrochemical Society*, 153 (2006), 2, pp. A329-A333 DOI: 10.1149/1.2139955
- [36] Huang, P., *et al.*, Experimental and Modeling Analysis of Thermal Runaway Propagation Over the Large Format Energy Storage Battery Module with Li₄Ti₅O₁₂ Anode, *Applied Energy*, 183 (2016), pp. 659-673 DOI: 10.1016/j.apenergy.2016.08.160
- [37] Jia, Y., *et al.*, Thermal Runaway Propagation Behavior Within 18,650 Lithium-ion Battery Packs: A Modeling Study, *Journal of Energy Storage*, 31 (2020), pp. 101668 DOI:

10.1016/j.est.2020.101668

- [38] Choi, J., *et al.*, Enhancement of Thermal Stability and Cycling Performance in Lithium-ion Cells Through the Use of Ceramic-coated Separators, *Journal of Power Sources*, 195 (2020), 18, pp. 6192-6196 DOI: 10.1016/j.jpowsour.2009.11.020
- [39] Jung, Y.C., *et al.*, Ceramic Separators Based on Li-conducting Inorganic Electrolyte for High-performance Lithium-ion Batteries with Enhanced Safety, *Journal of Power Sources*, 291 (2015), pp. 675-683 DOI: 10.1016/j.jpowsour.2015.06.001
- [40] Deng, Y., *et al.*, Al₂O₃/PVdF-HFP-CMC/PE Separator Prepared Using Aqueous Slurry and Post-hot-pressing Method for Polymer Lithium-ion Batteries with Enhanced Safety, *Electrochimica Acta*, 212 (2016), pp. 416-425 DOI: 10.1016/j.electacta.2016.07.016
- [41] Jung, B., *et al.*, Thermally Stable Non-aqueous Ceramic-coated Separators with Enhanced Nail Penetration Performance, *Journal of Power Sources*, 427 (2019), pp. 271-282 DOI: 10.1016/j.jpowsour.2019.04.046
- [42] Meng, F., *et al.*, Enhanced Safety Performance of Automotive Lithium-ion Batteries with Al₂O₃ Coated Non-woven Separator, *Batteries & Supercaps*, 4 (2021), 1, pp. 146-151 DOI: 10.1002/batt.202000169
- [43] Chou, L.Y., *et al.*, Electrolyte-Resistant Dual Materials for the Synergistic Safety Enhancement of Lithium-Ion Batteries, *Nano Letters*, 21 (2021), 5, pp. 2074-2080 DOI: 10.1021/acs.nanolett.0c04568
- [44] Zhang, T., *et al.*, Thermal Runaway Propagation Characteristics and Preventing Strategies Under Dynamic Thermal Transfer Conditions for Lithium-ion Battery Modules, *Journal of Energy Storage*, 58 (2023), pp. 106463 DOI: 10.1016/j.est.2022.106463
- [45] Lamb, J., *et al.*, Failure Propagation in Multi-cell Lithium Ion Batteries, *Journal of Power Sources*, 283 (2015), pp. 517-523 DOI: 10.1016/j.jpowsour.2014.10.081
- [46] Zaghib, K., *et al.*, Enhanced Thermal Safety and High Power Performance of Carbon-coated LiFePO₄ Olivine Cathode for Li-ion Batteries, *Journal of Power Sources*, 219 (2012), pp. 36-44 DOI: 10.1016/j.jpowsour.2012.05.018
- [47] Kong, D., *et al.*, Numerical Investigation of Thermal Runaway Behavior of Lithium-ion Batteries with Different Battery Materials and Heating Conditions, *Applied Thermal Engineering*, 189 (2021), pp. 116661 DOI: 10.1016/j.applthermaleng.2021.116661

RECEIVED DATE: 2.04.2023

DATE OF CORRECTED PAPER: 13.05.2023

DATE OF ACCEPTED PAPER: 2.08.2023.